

# Characterization of a Novel Variable Friction Connection for Semi-Active Cladding System

Yongqiang Gong<sup>1</sup>, Liang Cao<sup>1</sup>, Simon Laflamme<sup>1,2</sup>, Spencer Quiel<sup>3</sup>, James Ricles<sup>3</sup>, Douglas Taylor<sup>4</sup>

---

## Abstract

Cladding systems are conventionally designed to serve architectural purposes and protect occupants from the environment. Some research has been conducted in altering the cladding system in order to provide additional protection against natural and man-made hazards. The vast majority of these solutions are passive energy dissipators, applicable to the mitigation of single types of hazards. In this paper, we propose a novel semi-active variable friction device that could act as a connector linking a cladding panel to the structural system. Because of its semi-active capabilities, the device, here termed variable friction cladding connection (VFCC), could be utilized to mitigate different hazards, either considered individually or combined, also known as multi-hazards. The VFCC consists of two sets of sliding friction plates onto which a variable normal force can be applied through an actuated toggle system. A static model is derived to relate the device's Coulomb friction force to the actuator stroke. This model is integrated into a dynamic friction model to characterize the device's dynamic behavior. A prototype of the VFCC is constructed using 3D printing. The prototype is tested under harmonic excitations to identify the model parameters and characterized on a set of non-stationary excitations under different actuator stroke lengths. Results show good agreement between the model and experimental data, demonstrating that the device functions as-designed.

*Keywords:* Semi-active damper; Variable friction; Cladding connection; Multi-hazard mitigation; High performance control systems; 3D printing.

---

## 1. Introduction

Performance-based design (PBD) of civil structures is a design strategy that consists of sizing structural stiffness and supplemental damping in order to restrict structural motion to prescribed levels of performance. Often, PBD leads to substantial savings on materials by enabling lighter structural systems, and also provides enhanced protection against natural and man-made hazards as well as more uninterrupted serviceability [1]. However, in the case where there are multiple excitations either individually considered or combined, termed

---

<sup>1</sup>Department of Civil, Construction, and Environmental Engineering, Iowa State University, Ames, IA 50011, U.S.A

<sup>2</sup>Department of Electrical and Computer Engineering, Iowa State University, Ames, IA 50011, U.S.A

<sup>3</sup>Department of Civil and Environmental Engineering, Lehigh University, Bethlehem, PA 18015, U.S.A

<sup>4</sup>Taylor Devices, North Tonawanda, NY 14120, U.S.A

multi-hazards, a PBD approach becomes difficult to implement because it requires a high level of redundancy, as discussed in early research on passive mitigation of multi-hazards [2, 3]. In particular, passive supplemental energy dissipation systems typically have limited performance bandwidth [4, 5], and are therefore restrained to achieving the prescribed performance for single types of hazards.

Alternatively, one can utilize semi-active, hybrid, and active structural control systems, here termed high performance control systems (HPCS). HPCS have been proposed due to their potential to substantially enhance structural performance in comparison with traditional passive mitigation systems, as they can perform over a wide excitation bandwidth, ideal for multi-hazard mitigation. Examples of HPCS can be found in Refs. [1, 6, 7]. These devices include variable fluid, variable stiffness, variable orifice, and variable friction mechanisms.

Here we propose a novel semi-active modified friction cladding connection, termed variable friction cladding connection (VFCC), that leverages the motion of cladding to reduce the effects of natural and made-made hazards on the structural system. Early work on structural control using cladding panels includes double-layer foam cladding [8], tube-core cladding [9], and sacrificial panels composed of foam-based materials [10, 11, 12], all geared towards mitigation of blast loads. A considerable challenge with these panels is their low performance versus low-frequency loads and their relatively high costs. Energy dissipation through cladding connections have also been considered. Goodno *et al.* [13] studied ductile connections to dissipate energy through plastic deformations and therefore reduce inter-story drift. Baird *et al.* [14] explored a U-shaped flexural plates connection to passively dissipate seismic energy. Mannetes and Mermari [15] reviewed utilizations of cladding panel systems as energy dissipators for seismic loads. Amadio and Bedon [16] proposed a viscoelastic spider connection for mitigating blast loads.

All of the surveyed energy dissipation mechanisms based on cladding panels or connections are passive dissipation strategies. Instead, the proposed VFCC is designed for multi-hazard mitigation. Its mechanism is based on variable friction. Various HPCS based on variable friction have been explored for structural control applications. Their variable control force is based on a variable normal force applied onto a sliding interface. Examples of variable friction devices in literature include electromagnetic- [17], electromechanical- [18, 19], hydraulic- [20, 21], piezoelectric- [22, 23, 24, 25, 26], pneumatic- [27, 28], and magnetorheological- [29, 30, 31] based technologies.

The VFCC is designed to dissipate energy through two sets of sliding plates connecting cladding to the structural frame. Friction is produced by an actuator that varies the normal force on the sliding plates via a toggle system. The mechanism is designed to provide protection against blast and for daily operations when it is in a passive mode. It can be actuated to provide wind and seismic resistance through strategically varying the normal force via a feedback system. This paper introduces the VFCC as an alternative to traditional cladding connections, potentially transforming traditional cladding panels into multifunction systems capable

of maintaining architectural feature while providing enhanced structural resiliency. A dynamic model for the VFCC is developed and experimentally verified on a 3D printed prototype.

The paper is organized as follows. Section 2 provides the theoretical background on the variable friction connection. Section 3 presents the dynamic model of the semi-active damper. Section 4 identifies the dynamic model parameters using the response of the VFCC subjected to harmonic excitations under various levels of an applied normal force. Section 5 validates the tuned dynamic model of the prototype by subjecting the VFCC to non-stationary excitations. Section 6 concludes the paper.

## 2. Variable Friction Cladding Connection

A schematic of the VFCC friction mechanism is shown in Fig. 1(a). It consists of two sets of friction plates onto which a normal force is applied via toggles. The device includes blocks preventing the toggles from moving beyond a vertical alignment when pushed. The variation in the normal force is provided by an actuator, which could either be hydraulic or pneumatic. A possible installation of the device is its embedment in a floor slab, transmitting the lateral force from the cladding system to the structural frame. A representative schematic of the installation within a floor slab is shown in Fig. 1(b). The device is engineered to include an impact rubber bumper to prevent the sliding friction plates from colliding (not shown in Fig. 1(b)).

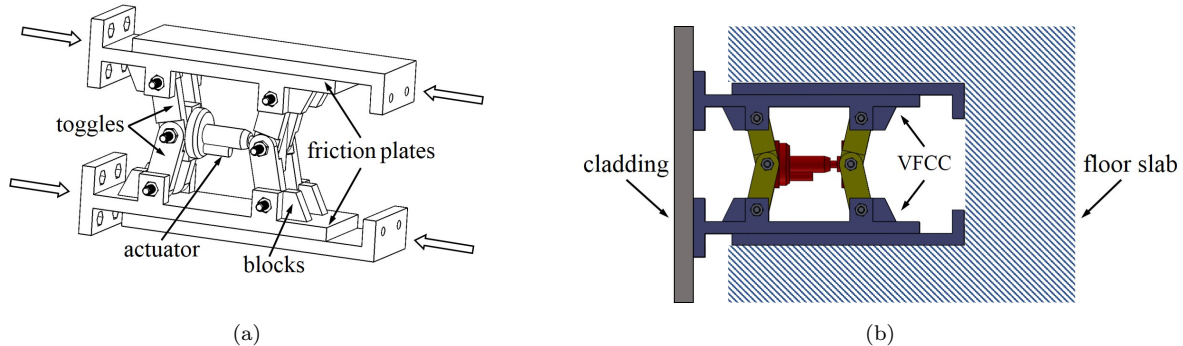


Figure 1: Schematic representation of the VFCC: (a) friction mechanism and (b) possible installation in a floor slab (top view).

The semi-active device is designed to achieve four different damping configurations:

1. Toggles fully locked, daily operations and blast loads. Both toggles are pushed vertically, leading to the device locking in a high friction mode. This is the passive mode, since no power input is required to maintain the toggles in the locked position. This configuration behaves as a rigid connector for daily operations and the system performs similar to any conventional cladding system with high stiffness. This configuration is also used to mitigate blast loads. Assuming that the cladding itself resists the

blast force, the impact force will exceed the static friction resulting in slippage of the connection, therefore dissipating blast energy through friction without delay.

2. Toggles semi-locked, extreme wind and seismic loads. The device performs as a variable friction damper under a control force. This particular configuration is employed to control interstory drift to limit damage to cladding (e.g. under extreme wind or seismic events).
3. Toggles retracted, high wind loads. The friction plates are fully disengaged, allowing the plate to slide freely, and the resistance provided by the connection is minimal. This configuration is also passive (no power input once the toggles are retracted), and can be used to limit acceleration transfer to floors.

### 2.1. Friction Mechanism

In what follows, the Coulomb friction force generated by the device is derived as a function of the actuator stroke. In the next section, a dynamic model building on these findings will be presented to characterize the device's behavior during sliding motion.

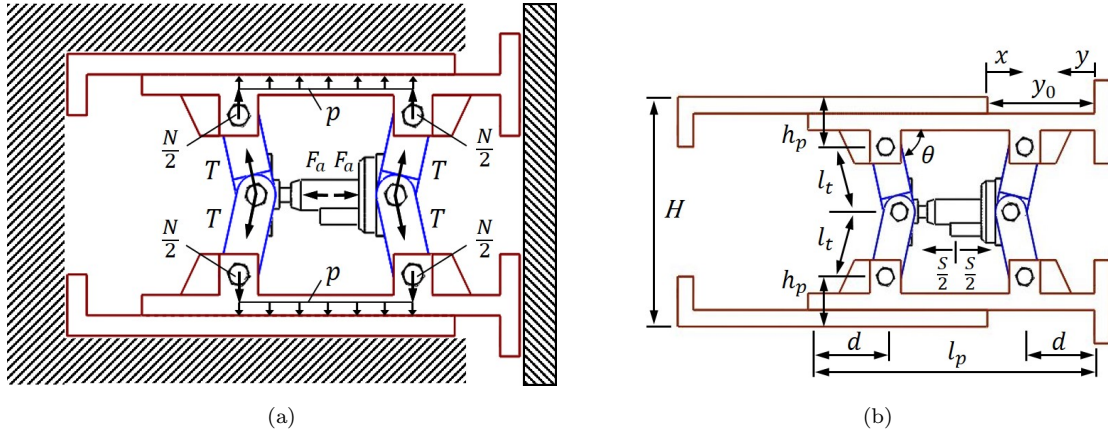


Figure 2: Schematic representation of the VFCC: (a) diagram of forces and (b) dimensional configuration.

The force diagram of the VFCC is illustrated in Fig. 2(a). The actuator force  $F_a$  generates an axial force  $T$  on the toggles, which in turn produces a normal force  $N$  on the friction plates. These forces are written

$$T = k_t \Delta l_t \quad (1)$$

$$N = k_p \Delta h_p \quad (2)$$

$$N = 2T \sin \theta \quad (3)$$

where  $k_t$  and  $k_p$  are the toggles and friction plates stiffnesses, respectively,  $\theta$  is the angle between toggle and plate as shown in Fig. 2(b); and  $\Delta l_t$  and  $\Delta h_p$  are the geometric deformations of the toggles and friction

plates, with

$$\Delta l_t = l_{t,0} - l_t \quad (4)$$

$$\Delta h_p = h_{p,0} - h_p \quad (5)$$

where  $l_t$  is the length of the toggles,  $h_p$  the thickness of the friction plates, and subscript 0 relates to the initial values. The distance  $H$  between the outer surfaces of both plates is given by

$$H = 2(h_p + l_t \sin \theta) \quad (6)$$

Since both the top and bottom friction plates are restrained (e.g., by a concrete slab),  $H$  remains constant and the deformation of the friction plates is written

$$\Delta h_p = l_t \sin \theta - l_{t,0} \sin \theta_0 \quad (7)$$

where  $\theta_0$  is the initial angle between the toggles and the friction plates. Substituting Eqs. (1) and (2) into Eq. (3) yields the following expression for  $\Delta h_p$

$$\Delta h_p = \frac{2k_t}{k_p} (l_{t,0} - l_t) \sin \theta \quad (8)$$

Using Eqs. (7) and (8) gives an expression for  $l_t$  as a function of  $\theta$ , where

$$l_t = l_{t,0} \left( \frac{k}{k_p} + \frac{k \sin \theta_0}{2k_t \sin \theta} \right) \quad (9)$$

with

$$k = \frac{2k_t k_p}{2k_t + k_p} \quad (10)$$

Similarly, an expression for  $h_p$  as a function of  $\theta$  can be obtained by substituting Eq. (9) into Eq. (7):

$$h_p = h_{p,0} - \frac{k}{k_p} l_{t,0} (\sin \theta - \sin \theta_0) \quad (11)$$

and an expression for  $N$  as a function of  $\theta$  using Eq. (11) and Eq. (2):

$$N = k l_{t,0} (\sin \theta - \sin \theta_0) \quad (12)$$

The geometric relationship between actuator stroke  $s$  and  $\theta$  can be given using Eq. (9):

$$\begin{aligned} s &= 2(l_{t,0} \cos \theta_0 - l_t \cos \theta) \\ &= 2l_{t,0} \left[ \cos \theta_0 - \frac{\sqrt{1 - \sin^2 \theta}}{\sin \theta} \left( \frac{k}{k_p} \sin \theta + \frac{k}{2k_t} \sin \theta_0 \right) \right] \end{aligned} \quad (13)$$

An expression relating  $N$  to  $s$  can be obtained using Eqs. (12) and (13)

$$\frac{\frac{N}{kl_{t,0}} + \sin \theta_0}{\frac{N}{k_pl_{t,0}} + \sin \theta_0} \left( \cos \theta_0 - \frac{s}{2l_{t,0}} \right) = \sqrt{1 - \left( \frac{N}{kl_{t,0}} + \sin \theta_0 \right)^2} \quad (14)$$

The device can be designed such that the stiffness of the sliding plates (along the direction of their thicknesses) is significantly larger than the stiffness of the toggles (along the direction of their length). In this case,  $k_t \ll k_p$ , and  $k$  can be approximated as

$$k = \frac{k_t}{\frac{k_t}{k_p} + \frac{1}{2}} \approx 2k_t \quad (15)$$

with Eqs. (12) and (13) simplifying to

$$N = 2k_t l_{t,0} (\sin \theta - \sin \theta_0) \quad (16)$$

$$s = 2l_{t,0} (\cos \theta_0 - \cot \theta \sin \theta_0) \quad (17)$$

and the relationship between  $N$  and  $s$  is written

$$N = 2k_t l_{t,0} \sin \theta_0 \left( \frac{1}{\sqrt{(\cos \theta_0 - \frac{s}{2l_{t,0}})^2 + \sin^2 \theta_0}} - 1 \right) \quad (18)$$

As illustrated in Fig. 2, the compressive pressure  $p$  on the friction plates generated by toggle forces  $T$  is assumed to be uniformly distributed between both toggles:

$$p = \frac{N}{A_c|_{\max}} \quad (19)$$

where  $A_c|_{\max} = b_p(l_p - 2d)$  is the maximum contact area of the friction plates under the normal pressure,  $l_p$  and  $b_p$  are the length and width of the friction plate, respectively, and  $d$  is the distance between the toggle and the end of the friction plate. The effective contact area of the friction plates under the normal pressure depends on the relative displacement between friction plates  $y$

with

$$A_c = \begin{cases} b_p(l_p - 2d) & \text{if } 0 \leq y < d \\ b_p(l_p - d - y) & \text{if } d \leq y \leq l_p - d \\ 0 & \text{if } l_p - d < y \leq l_p \end{cases} \quad (20)$$

The generated Coulomb friction force  $F$  is taken as proportional to the maximum contact area  $A_c|_{\max}$

$$F = 2\mu N \frac{A_c}{A_c|_{\max}} \quad (21)$$

or

$$F = \begin{cases} 2\mu N & \text{if } 0 \leq y < d \\ 2\mu N \frac{l_p - y - d}{l_p - 2d} & \text{if } d \leq y \leq l_p - d \\ 0 & \text{if } l_p - d < y \leq l_p \end{cases} \quad (22)$$

where  $\mu$  is the coefficient of friction.

### 3. Dynamic Model

In this section, a dynamic model is derived to characterize the behavior of the device under dynamic sliding motion. The LuGre friction model is selected due to its known simplicity and capability to model the Stribeck effect and rate dependent friction phenomena [32, 33]. Under the LuGre model, the friction force  $F_f$  is written

$$F_f(x) = \sigma_0 z + \sigma_1 \dot{z} + \sigma_2 \dot{x} \quad (23)$$

with

$$\begin{aligned} \dot{z} &= \dot{x} - \sigma_0 \frac{|\dot{x}|}{g(\dot{x})} z \\ g(\dot{x}) &= F_c + (F_s - F_c) e^{-(\dot{x}/\dot{x}_s)^2} \end{aligned} \quad (24)$$

where  $\sigma_0$ ,  $\sigma_1$ , and  $\sigma_2$  are constants representing the stiffness of the bristles, microdamping, and viscous friction, respectively,  $x$  is the sliding displacement of the inner friction plate and taken as  $x = y_0 - y$  with  $x = 0$  corresponding to the initial location of the sliding plates  $y_0$  as illustrated in Fig.2(b),  $\dot{x}$  the sliding velocity,  $\dot{x}_s$  a constant modeling the Stribeck velocity,  $z$  an evolutionary variable,  $g(\dot{x})$  a function that describes the Stribeck effect,  $F_c$  the Coulomb friction force and  $F_s$  the magnitude of the Stribeck effect.

Fig. 3 are plots of a typical dynamic response of the VFCC over a harmonic excitation (taken at 0.05 Hz,  $\pm 13$  mm (0.50 in), in the locked position ( $s = 20$  mm (0.80 in) or  $\theta = 90^\circ$ ), with  $y = 64 \pm 13$  mm ( $2.5 \pm 0.5$  in) corresponding to  $x = 0 \pm 13$  mm (0.5 in). With this configuration,  $d < y < l_p - d$  and the Coulomb friction force  $F_c$  can be written

$$F_c = \frac{l_p - d - y_0 + x}{l_p - d - y_0} F_{c,0} \quad (25)$$

with  $F_{c,0}$  representing the initial Coulomb friction force at  $x = 0$

$$F_{c,0} = 2\mu N \frac{l_p - d - y_0}{l_p - 2d} \quad (26)$$

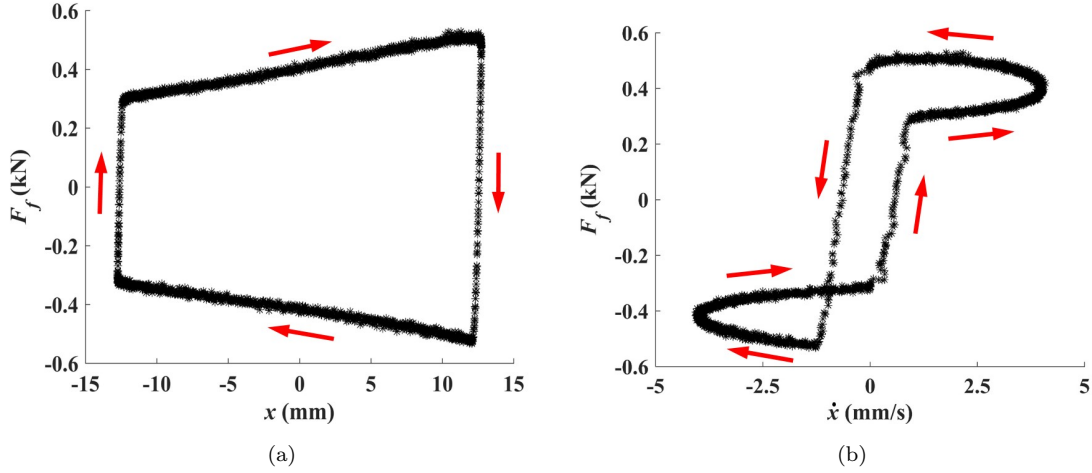


Figure 3: Dynamic response of the VFCC at 0.05 Hz,  $\pm 13$  mm ( $\pm 0.50$  in),  $s = 20$  mm (0.80 in) ( $\theta = 90^\circ$ ): (a) force-displacement (0.05 Hz) and (b) force-velocity (0.05 Hz).

The magnitude of the Stribeck effect  $F_s$  is modeled as proportional function of the Coulomb friction force  $F_c$

$$\begin{aligned} F_s &= \rho F_c \\ F_{s,0} &= \rho F_{c,0} \end{aligned} \quad (27)$$

where  $\rho > 1$  is a constant and  $F_{s,0}$  is the magnitude of the Stribeck effect at  $x = 0$ . In this representation, the initial Coulomb friction force varies with the actuator stroke  $s$ . An expression is obtained by substituting

$N$  from Eq. (18)

$$F_{c,0} = 4\mu k_t \frac{l_p - d - y_0}{l_p - 2d} l_{t,0} \sin \theta_0 \left( \frac{1}{\sqrt{(\cos \theta_0 - \frac{s}{2l_{t,0}})^2 + \sin^2 \theta_0}} - 1 \right) \quad (28)$$

$$= C_c \varphi(s)$$

with

$$\varphi(s) = l_{t,0} \sin \theta_0 \left( \frac{1}{\sqrt{(\cos \theta_0 - \frac{s}{2l_{t,0}})^2 + \sin^2 \theta_0}} - 1 \right) \quad (29)$$

In addition, previous investigations [20, 21] demonstrated that constant  $\sigma_0$  varies linearly with  $N$ . Here, for simplicity, we assume that  $\sigma_0$  varies linearly with  $s$  with

$$\sigma_0 = C_{\sigma_0} s + \sigma_0|_{s=0} \quad (30)$$

Lastly, also based on previous investigations, all other parameters are taken as independent on  $s$ , and none of the parameters depend on frequency.

#### 4. Identification of Model Parameters

The parameters of the dynamic models were identified on a prototype subjected to harmonic loadings. In what follows, the prototype is described, the testing methodology discussed, and results presented. The subsequent section will validate the identified model on non-stationary excitations.

##### 4.1. Prototype

A prototype of the VFCC was fabricated using 3D printing of an acrylonitrile butadiene styrene (ABS) polymer. The friction interfaces are steel-rubber, fabricated by adhering a steel pad onto each inner sliding surface and a rubber plate onto each outer sliding surface. A picture of the prototype mounted in an aluminum frame (for testing) is shown in Fig. 4(a) with its 3D printed components shown in Fig. 4(b), and its dimensions listed in Table 1. During test, the actuator stroke was emulated by using fixed spacers between both toggles.

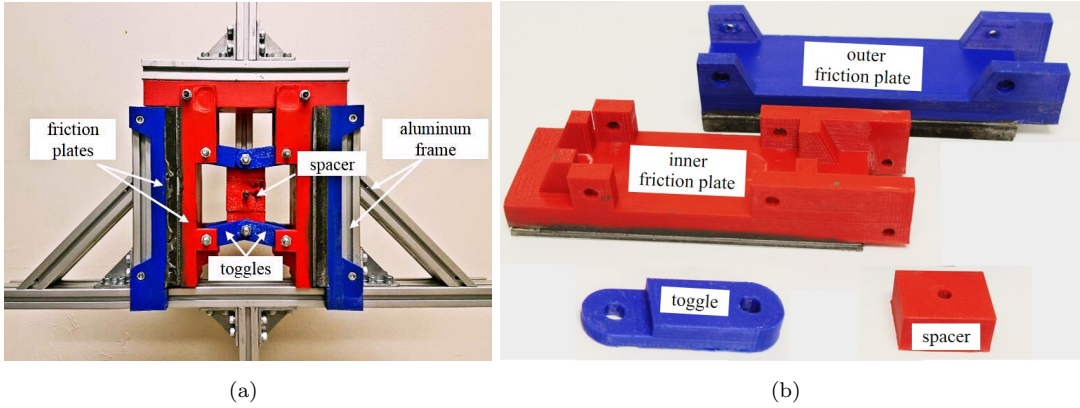


Figure 4: Picture of the VFCC: (a) prototype mounted in an aluminum frame for testing; and (b) 3D printed components of the prototype.

Table 1: Design parameters of the VFCC prototype.

parameter	variable	value	units
plate length	$l_p$	165 (6.50)	mm (in)
plate width	$b_p$	60 (2.36)	mm (in)
initial plates thickness	$h_{p,0}$	50 (1.97)	mm (in)
initial toggle length	$l_{t,0}$	40 (1.57)	mm (in)
toggle width	$b_t$	20 (0.79)	mm (in)
toggle thickness	$h_t$	10 (0.39)	mm (in)
toggle to plate end distance	$d$	45 (1.75)	mm (in)
outer plates distance	$H$	177 (6.98)	mm (in)
initial angle	$\theta_0$	1.32 (75.6)	rad ( $^\circ$ )
initial relative plate displacement	$y_0$	64 (2.50)	mm (in)

#### 4.2. Methodology

The prototype was mounted in an aluminum frame to restrain the outer sliding friction plates, and the frame installed in a 500 kN (110 k) Servo Hydraulic Material Testing Machine 810. Force and displacement data were obtained from a data acquisition system at 100 Hz. The device was subjected to a displacement-controlled harmonic load during two hours to first wear the lining surfaces in both the forward and backward directions in order to provide a constant surface throughout the sliding areas.

After this preparation, the VFCC was subjected to five cycles of displacement-controlled harmonic load of 13 mm (0.50 in) amplitude at 0.05 and 0.2 Hz. These tests were repeated under actuator stroke lengths  $s$  from 0 to 20 mm (0.80 in) in 2 mm (0.08 in) increments. A stroke  $s = 0$  ( $\theta = \theta_0$ ) in the tested configuration was

set such that friction plates were barely in contact, while  $s = 20$  mm (0.80 in) provides a fully locked position ( $\theta = 90^\circ$ ). The initial position  $x = 0$  mm provides an average effective contact area  $A_{c,0} = b_p(l_p - d - y_0)$  under normal pressure, and  $x_{\max} = 13$  mm (0.50 in) corresponds to the maximum effective contact area  $A_{c,\max} = b_p(l_p - d - y_0 + x_{\max})$ .

#### 4.3. Results

First, constants  $C_c$  and  $\rho$  are determined from experimental test data. Fig. 5(a) is a plot of the experimental values obtained for  $C_c = F_{c,0}/\varphi$  as a function of  $s$ , while Fig. 5(b) is a plot of the experimental values obtained for  $\rho = F_{s,0}/F_{c,0}$ . In both cases, the experimental value can be modeled by a constant (linear fit), except for lower values of the actuator stroke ( $s \leq 4$  mm), which could be attributed to an irregular behavior occurring when the normal force  $N$  applied onto the sliding plates is low.

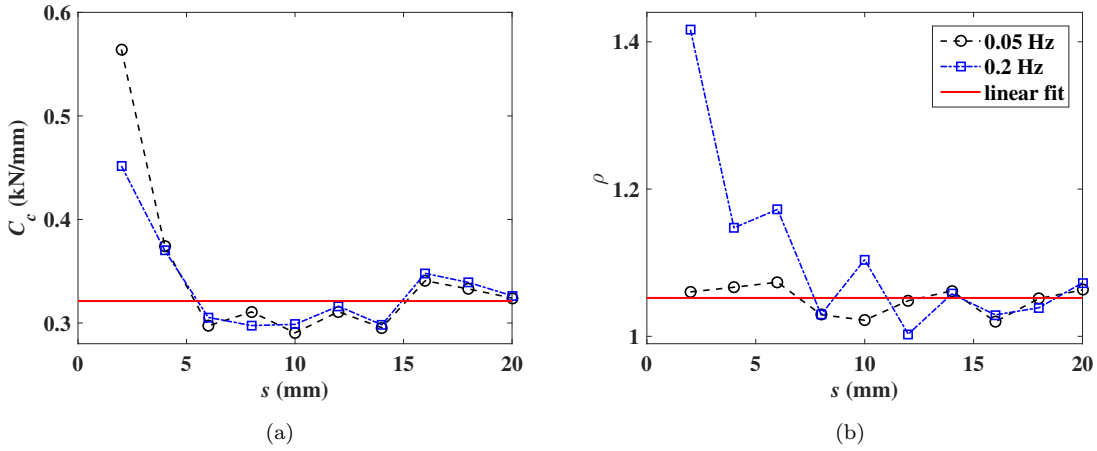


Figure 5: Identification of model constants (a)  $C_c$ ; and (b)  $\rho$ .

Second, values obtained for  $C_c$  and  $\rho$  are integrated in the dynamic model, and parameters  $\sigma_0$ ,  $\sigma_1$ , and  $\sigma_2$  identified by minimizing the error function  $J$ :

$$J_i = \|\hat{F}_{f,i} - F_{f,i}\|_2 \quad (31)$$

where  $F_f$  is the friction force measured experimentally,  $\hat{F}_f$  the friction force estimated by the model,  $i$  is a test associated with a given actuator stroke length  $s$ , and  $\|\cdot\|_2$  is the Euclidean norm. The dependence of  $\sigma_0$  on  $s$  is estimated using the command `lsqcurvefit` in MATLAB. Fig. 6 is a plot of the estimated values for  $\sigma_0$ , along with a linear fit yielding values for  $C_{\sigma_0}$  and  $\sigma_0|_{s=0}$ . Table 2 summarizes the identified model parameters.

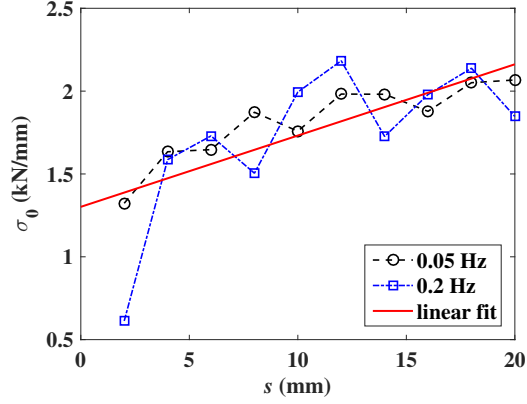


Figure 6: Plot of  $\sigma_0$  versus  $s$ .

Table 2: Identified model parameters.

parameter	units	value
$\rho$	–	1.052
$C_c$	$\text{kN} \cdot \text{mm}^{-1}$ ( $\text{kip} \cdot \text{in}^{-1}$ )	0.321 (1.834)
$C_{\sigma_0}$	$\text{kN} \cdot \text{mm}^{-2}$ ( $\text{kip} \cdot \text{in}^{-2}$ )	0.043 (6.240)
$\sigma_0 _{s=0}$	$\text{kN} \cdot \text{mm}^{-1}$ ( $\text{kip} \cdot \text{in}^{-1}$ )	1.302 (7.432)
$\sigma_1$	$\text{N} \cdot \text{s} \cdot \text{mm}^{-1}$ ( $\text{lb} \cdot \text{s} \cdot \text{in}^{-1}$ )	0.200 (1.142)
$\sigma_2$	$\text{N} \cdot \text{s} \cdot \text{mm}^{-1}$ ( $\text{lb} \cdot \text{s} \cdot \text{in}^{-1}$ )	0.200 (1.142)

Figs. 7 and 8 show the experimental data fitting using the model based on the identified parameters listed in Table 2. Plots show the force-displacement and force-velocity loops for two representative stroke lengths:  $s = 12$  mm (0.48 in) which represents an unlocked and average actuated stroke length, and  $s = 20$  mm (0.80 in) which represents the locked position. There is good agreement between experimental data and model values. A higher level of noise occurs under the higher excitation frequency (0.2 Hz) and larger actuator stroke ( $s = 20$  mm (0.80 in)), which could be attributed to chattering. Fig. 9 are plots of the force-displacement and force-velocity loops obtained from the dynamic model for a harmonic excitation of 13 mm (0.50 in) at 0.05 Hz under various levels of actuator stroke.

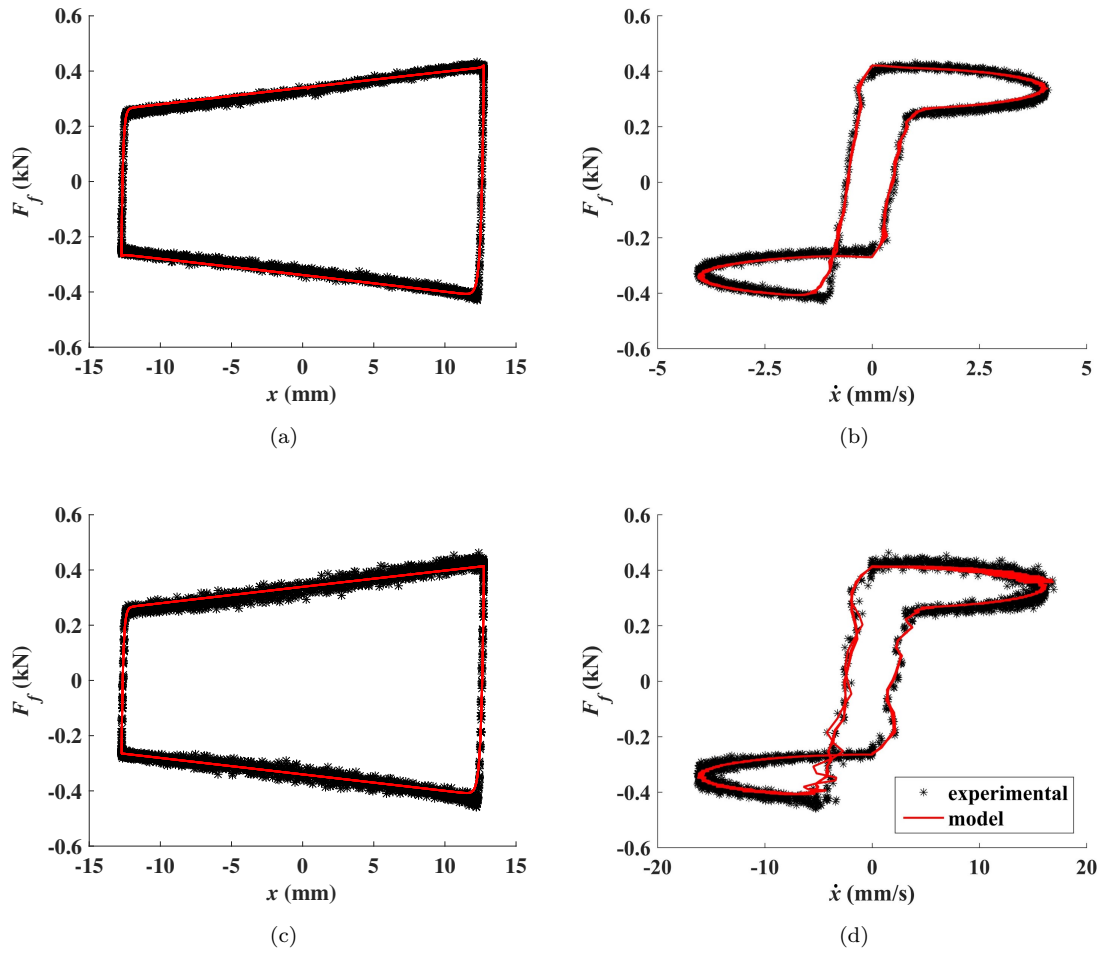


Figure 7: Harmonic test at stroke length  $s = 12$  mm (0.48 in) (unlocked position): (a) force-displacement (0.05 Hz); (b) force-velocity (0.05 Hz); (c) force-displacement (0.2 Hz); and (d) force-velocity (0.2 Hz).

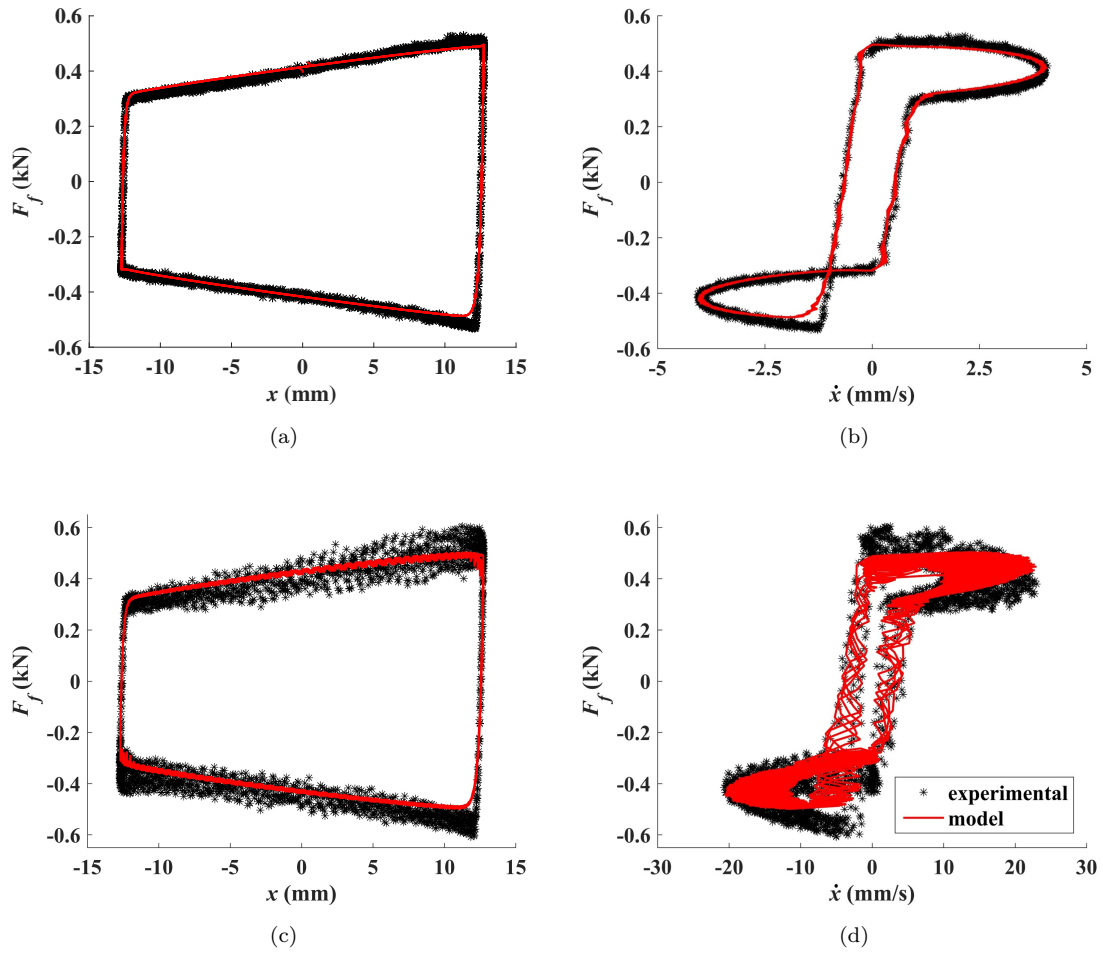


Figure 8: Harmonic test at stroke length  $s = 20$  mm (0.80 in) (locked position): (a) force-displacement (0.05 Hz); (b) force-velocity (0.05 Hz); (c) force-displacement (0.2 Hz); and (d) force-velocity (0.2 Hz).

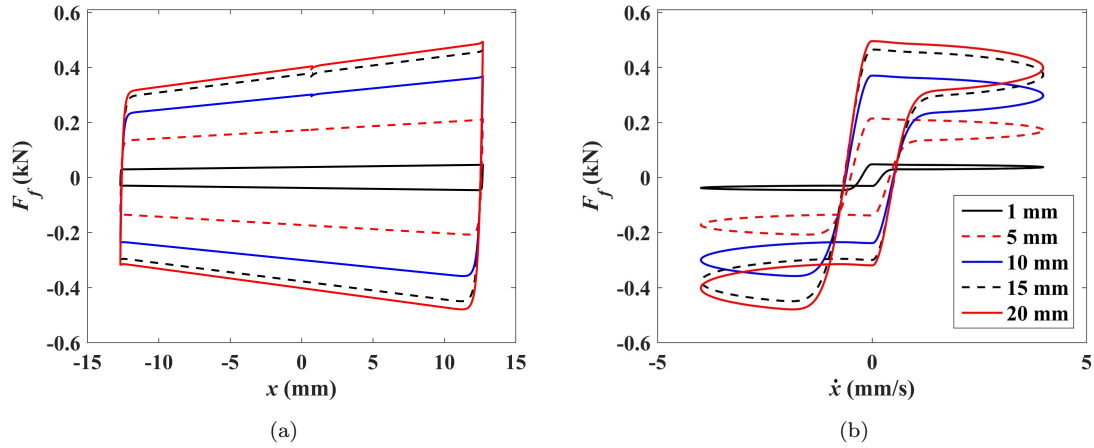


Figure 9: (a) Force-displacement and (b) force velocity loops for a harmonic excitation of 13 mm (0.50 in) at 0.05 Hz.

## 5. Model validation under non-stationary excitations

The tuned dynamic friction model is validated using a methodology similar to [20]. The methodology consists of directly subjecting the device to seismic excitations due to their rich frequency content and varying amplitudes, representing an extreme input for verification purposes. Note that a direct seismic excitation input does not necessarily represent the excitation on the device installed into a structural frame, but gives a useful indication of the device's dynamic performance under a non-stationary excitation. The seismic excitations are the 1979 Imperial Valley earthquake and the 1961 Hollister earthquake. The excitation records were obtained from USGS Station 5155 and USGS Station 1028, respectively, extracted from the PEER ground motion record database [34]. Ground displacements were computed by double integrating the ground acceleration data and scaled to a maximum of 10.2 mm (0.4 in) to match the limitations of the testing equipment at high frequencies. The acceleration and scaled displacement time histories are shown in Fig. 10.

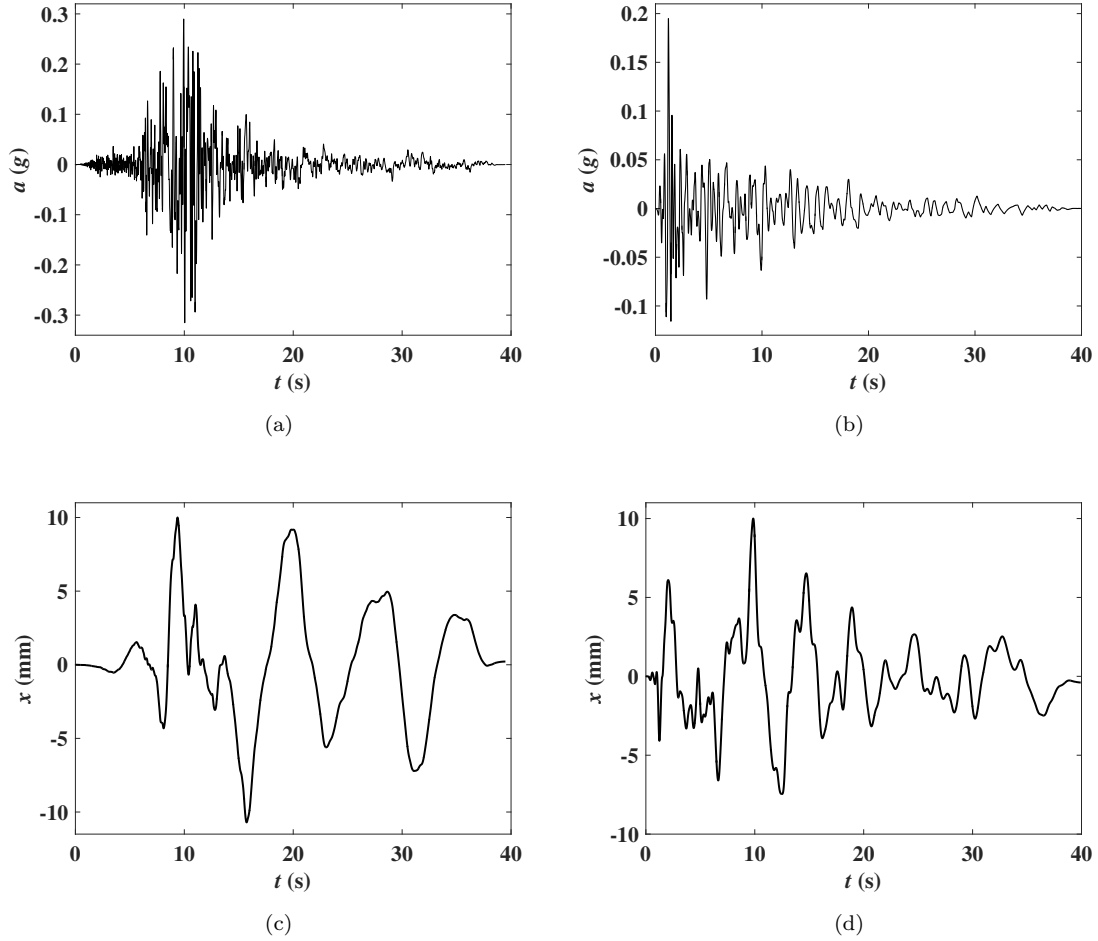


Figure 10: Earthquake input excitations: (a) unscaled ground acceleration (Imperial Valley earthquake); (b) unscaled ground acceleration (Hollister earthquake); (c) scaled ground displacement (Imperial Valley earthquake); and (d) scaled ground displacement (Hollister earthquake).

Figs. 11 to 14 show the experimental data fitting for each seismic excitation under two representative strokes ( $s = 12$  mm (0.48 in) and  $s = 20$  mm (0.80 in)). There is good agreement between the experimental data and the values estimated from the model. The fit of the response to the Imperial Valley earthquake under  $s = 12$  mm (0.48 in) shows a significant underestimation at the end of the time series (Fig. 11(a)), which can be attributed to a residual force in the testing machine at the end of the test. This phenomenon is not observed in other results. In addition, there is a small disagreement in the fit at higher stroke (Figs. 13 and 14) when the motion reverses (bottom-right corner of the force-displacement loops). This is attributable to a small asymmetry in the VFCC that becomes more apparent under higher friction forces, where the forward and backward forces differ. This asymmetry in forces could be reduced by additional wearing of the friction plates.

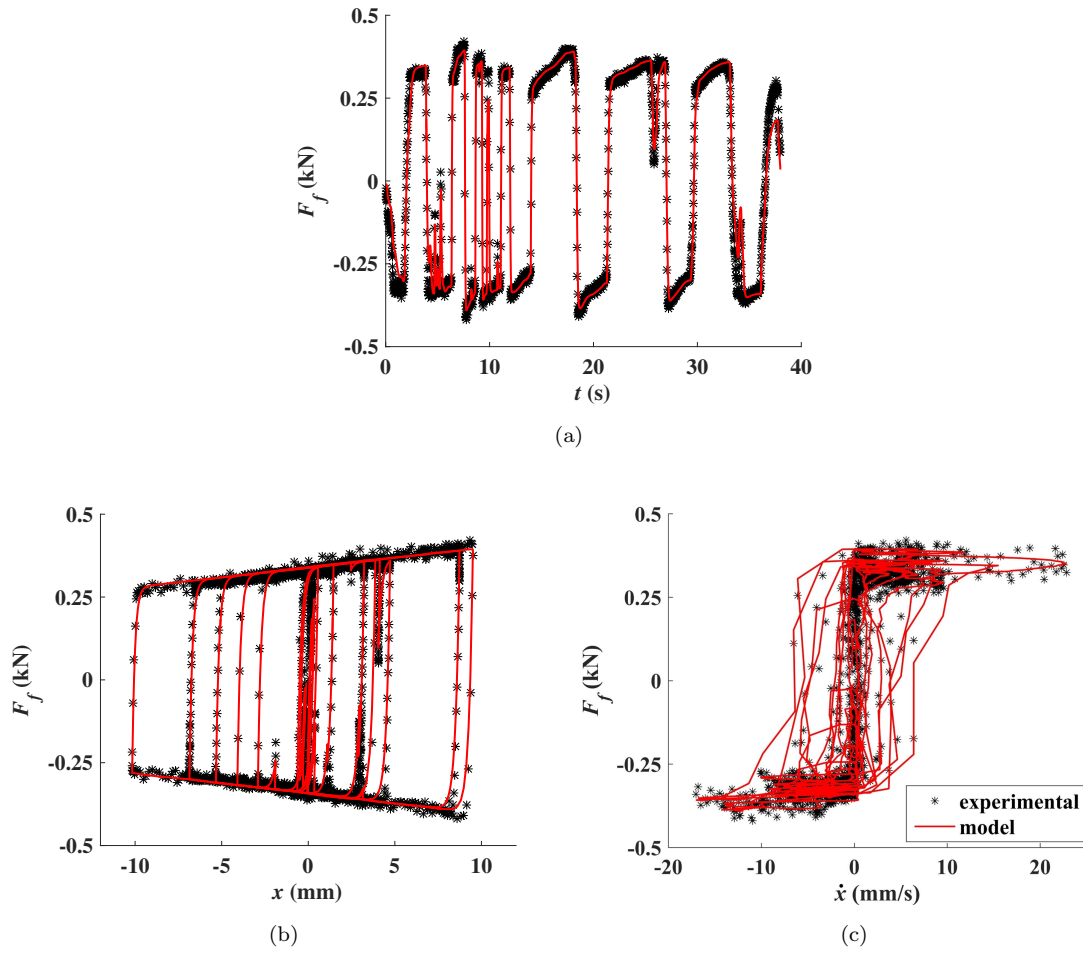


Figure 11: Imperial Valley earthquake at unlocked condition ( $s = 12$  mm (0.48 in)): (a) time history of damping force; (b) force-displacement loop; and (c) force-velocity loop.

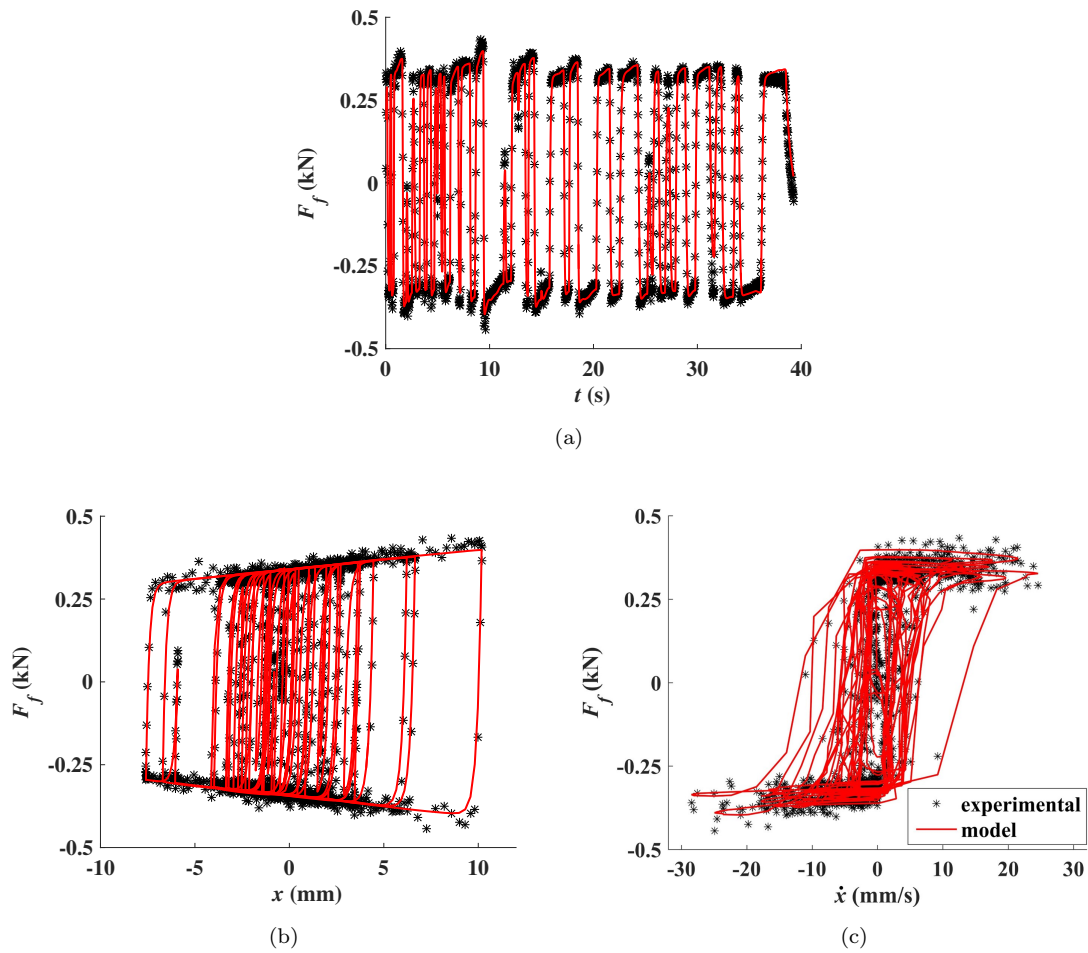


Figure 12: Hollister earthquake at unlocked condition ( $s = 12$  mm (0.48 in)): (a) time history of damping force; (b) force-displacement loop; and (c) force-velocity loop.

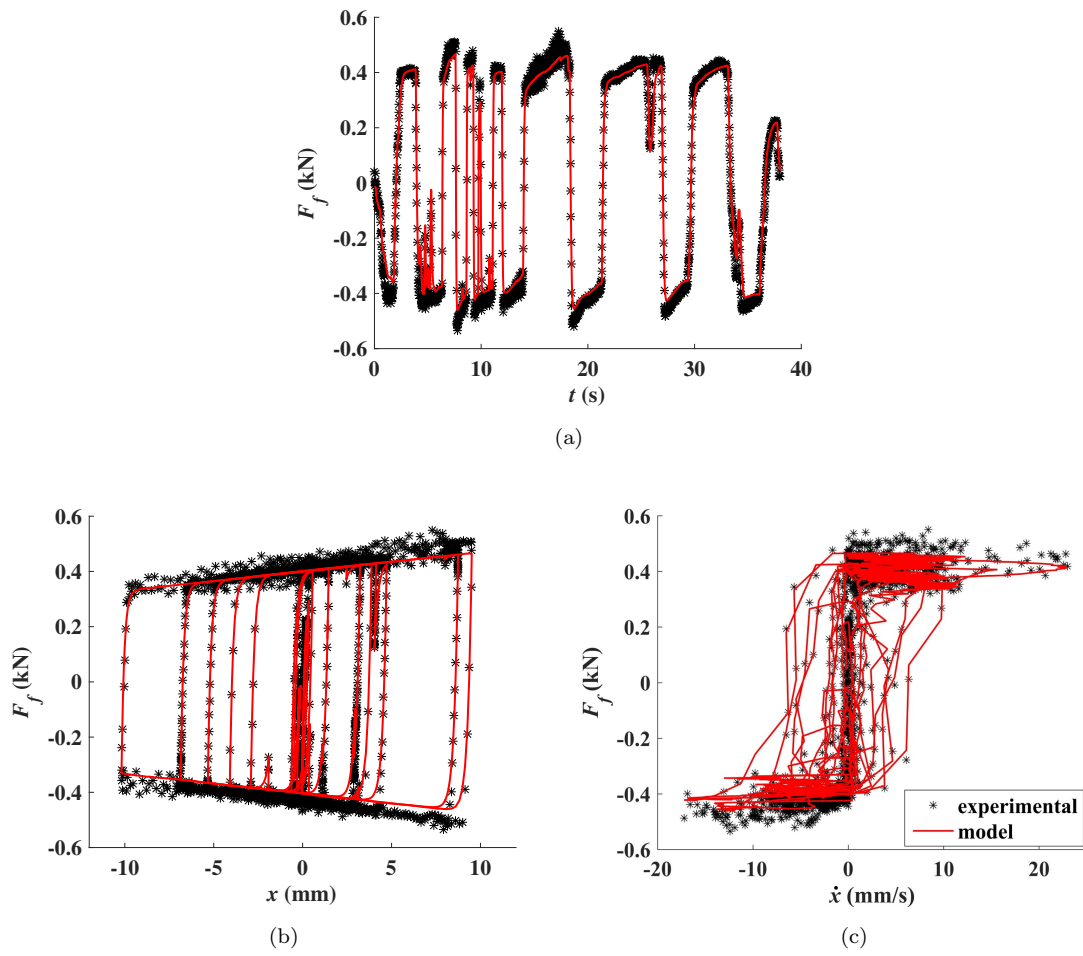


Figure 13: Imperial Valley earthquake at locked condition ( $s = 20$  mm (0.80 in)): (a) time history of damping force; (b) force-displacement loop; and (c) force-velocity loop.

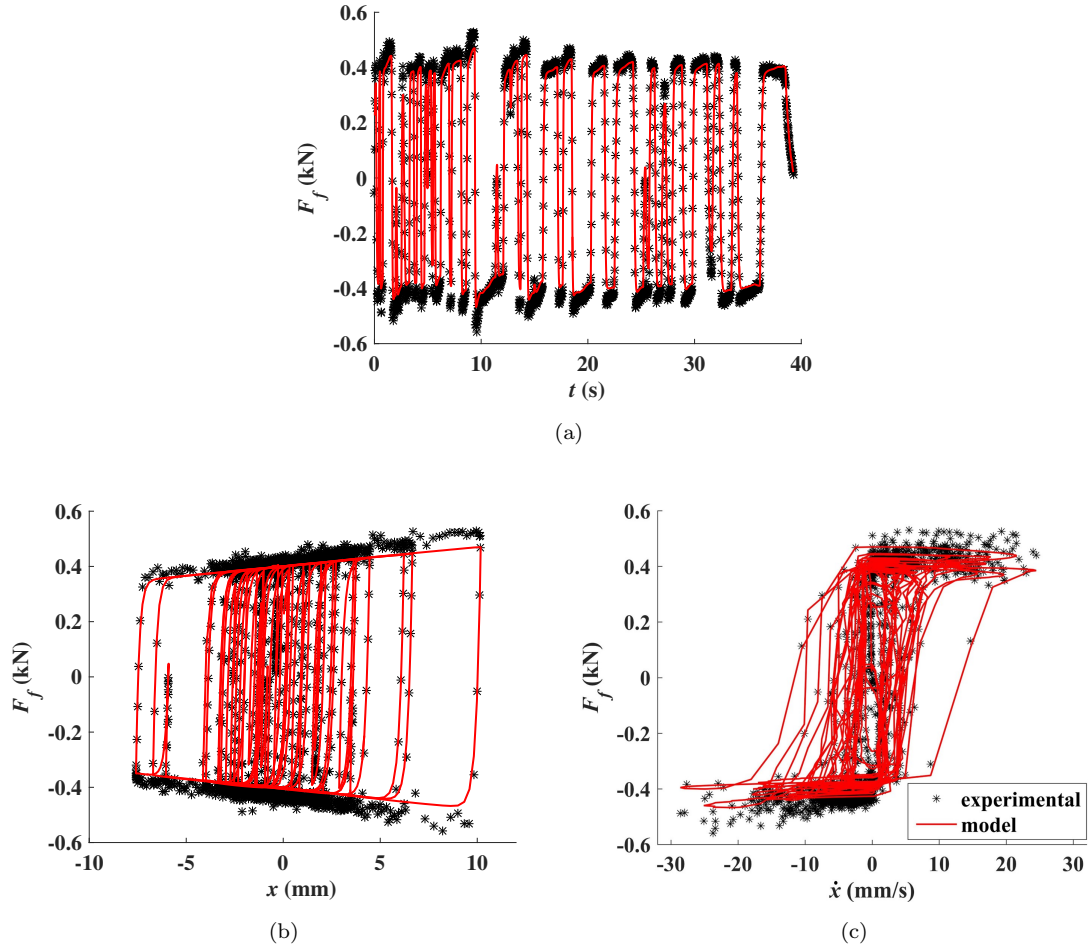


Figure 14: Hollister earthquake at locked condition ( $s = 20$  mm (0.80 in)): (a) time history of damping force; (b) force-displacement loop; and (c) force-velocity loop.

## 6. Conclusion

This paper introduced a novel semi-active friction device for connecting a cladding panel to the structural system. The device, termed the variable friction cladding connection (VFCC), was designed to mitigate different types of hazards. It consists of two sets of sliding friction plates onto which a variable normal force can be applied through an actuated toggle system. In a locked position, which is also its passive mode, the device provides a maximum friction resistance, therefore providing mitigation capabilities versus blast. It can also be entirely disengaged or actuated in order to mitigate earthquake and wind excitations.

A static model was derived to obtain an expression relating the Coulomb friction force to the actuator stroke. This relationship was then used within a dynamic friction model to characterize the dynamic behavior of the device. A prototype VFCC was fabricated using 3D printing and tested to identify the model

parameters using harmonic loadings. The tuned dynamic model was validated on non-stationary excitations under various actuator stroke. Results from the harmonic loadings showed that the dynamic model agreed with the experimental data. Results from the non-stationary excitations demonstrated good performance of the model at estimating the response of the VFCC, despite a slight disagreement between the model and experimental data under high actuator stroke that occurred when the sliding direction reversed. This disagreement was attributed to asymmetries in the prototype.

The model and experimental results presented in this paper demonstrated that the device could function as designed for providing variable friction capabilities to a cladding connection. Combined with a proper performance-based design methodology and a controller, the VFCC could have great potential at mitigating multi-hazards, either individually or combined. Future work includes testing of the integrated VFCC into a semi-active cladding system resisting blast, wind, and seismic loads, and developing performance-based design methodologies.

## ACKNOWLEDGMENTS

This material is based upon work supported by the National Science Foundation under Grant No. 1493497. Their support is gratefully acknowledged. Any opinions, findings, and conclusions or recommendations expressed in this material are those of the authors and do not necessarily reflect the views of the National Science Foundation. The authors are also indebted to Dr. Joseph A. Schaefer from the Department of Aerospace Engineering at Iowa State University for his help with the experiments.

## References

- [1] J. Connor, S. Laflamme, Structural motion engineering, Springer, 2014.
- [2] S. Dogruel, G. Dargush, Risk-based multi-hazard optimization of passively damped structures using evolutionary algorithms, in: Proceedings of The 14th World Conference on Earthquake Engineering October 12-17, 2008, Beijing, China, 2008.
- [3] J. Crawford, D. Houghton, J. Karns, Multi-hazard mitigation in steel frame air traffic control towers as a function of redundancy, lateral configuration and connection geometry, in: All-Regional FAA Structural Seminar on Seismic and Progressive Collapse Resistant Structures for Air Traffic Control Towers, 2002.
- [4] J. N. Yang, A. K. Agrawal, Semi-active hybrid control systems for nonlinear buildings against near-field earthquakes, *Engineering Structures* 24 (3) (2002) 271–280.
- [5] S. Laflamme, J. E. Slotine, J. Connor, Self-organizing input space for control of structures, *Smart Materials and Structures* 21 (11) (2012) 115015.

- [6] B. Spencer Jr, S. Nagarajaiah, State of the art of structural control, *Journal of structural engineering* 129 (7) (2003) 845–856.
- [7] F. Ubertini, G. Comanducci, S. Laflamme, A parametric study on reliability-based tuned-mass damper design against bridge flutter, *Journal of Vibration and Control* (2015) 1077546315595304.
- [8] G. Ma, Z. Ye, Energy absorption of double-layer foam cladding for blast alleviation, *International Journal of Impact Engineering* 34 (2) (2007) 329–347.
- [9] M. Theobald, G. Nurick, Experimental and numerical analysis of tube-core claddings under blast loads, *International Journal of Impact Engineering* 37 (3) (2010) 333–348.
- [10] C. Wu, L. Huang, D. J. Oehlers, Blast testing of aluminum foam-protected reinforced concrete slabs, *Journal of Performance of Constructed Facilities* 25 (5) (2010) 464–474.
- [11] C. Shim, N. Yun, R. Yu, D. Byun, Mitigation of blast effects on protective structures by aluminum foam panels, *Metals* 2 (2) (2012) 170–177.
- [12] R. Merrett, G. Langdon, M. Theobald, The blast and impact loading of aluminium foam, *Materials & Design* 44 (2013) 311–319.
- [13] B. Goodno, J. Craig, L. El-Gazairly, C. Hsu, Use of advanced cladding systems for passive control of building response in earthquakes, in: *Proceedings, 10th World Conference on Earthquake Engineering*, July, 1992, pp. 19–24.
- [14] A. Baird, A. Palermo, S. Pampanin, Controlling seismic response using passive energy dissipating cladding connections, in: *2013 NZSEE Conference*, 2013.
- [15] H. Maneetes, A. M. Memari, Introduction of an innovative cladding panel system for multi-story buildings, *Buildings* 4 (3) (2014) 418–436.
- [16] C. Amadio, C. Bedon, Viscoelastic spider connectors for the mitigation of cable-supported façades subjected to air blast loading, *Engineering Structures* 42 (2012) 190–200.
- [17] A. Agrawal, J. Yang, A semi-active electromagnetic friction damper for response control of structures, *Advanced technology in structural engineering* (2000) 1–8.
- [18] S. Narasimhan, S. Nagarajaiah, Smart base isolated buildings with variable friction systems: H controller and saivf device, *Earthquake engineering & structural dynamics* 35 (8) (2006) 921–942.
- [19] Y. Kawamoto, Y. Suda, H. Inoue, T. Kondo, Electro-mechanical suspension system considering energy consumption and vehicle manoeuvre, *Vehicle System Dynamics* 46 (S1) (2008) 1053–1063.

- [20] L. Cao, A. Downey, S. Laflamme, D. Taylor, J. Ricles, Variable friction device for structural control based on duo-servo vehicle brake: Modeling and experimental validation, *Journal of Sound and Vibration* 348 (2015) 41–56.
- [21] A. Downey, L. Cao, S. Laflamme, D. Taylor, J. Ricles, High capacity variable friction damper based on band brake technology, *Engineering Structures* 113 (2016) 287–298.
- [22] C. Ng, Y. Xu, Semi-active control of a building complex with variable friction dampers, *Engineering Structures* 29 (6) (2007) 1209–1225.
- [23] G. Chen, G. T. Garrett, C. Chen, F. Y. Cheng, Piezoelectric friction dampers for earthquake mitigation of buildings: design, fabrication, and characterization, *Structural Engineering and Mechanics* 17 (3.4) (2004) 539–556.
- [24] M. Unsal, C. Niezrecki, C. Crane III, A new semi-active piezoelectric-based friction damper, in: *Smart structures and materials*, International Society for Optics and Photonics, 2003, pp. 413–420.
- [25] L.-Y. Lu, G.-L. Lin, A theoretical study on piezoelectric smart isolation system for seismic protection of equipment in near-fault areas, *Journal of Intelligent Material Systems and Structures* 20 (2) (2009) 217–232.
- [26] J. Pardo-Varela, J. Llera, A semi-active piezoelectric friction damper, *Earthquake Engineering & Structural Dynamics* 44 (3) (2015) 333–354.
- [27] T. Vesselenyi, S. Dziac, I. Dziac, M.-J. Manolescu, Fuzzy and neural controllers for a pneumatic actuator, *International Journal of Computers Communications & Control* 2 (4) (2007) 375–387.
- [28] A. Mehmood, S. Laghrouche, M. El Bagdouri, Modeling identification and simulation of pneumatic actuator for vgt system, *Sensors and Actuators A: Physical* 165 (2) (2011) 367–378.
- [29] S. S. Sahasrabudhe, S. Nagarajaiah, Semi-active control of sliding isolated bridges using mr dampers: an experimental and numerical study, *Earthquake engineering & structural dynamics* 34 (8) (2005) 965–983.
- [30] M. A. Karkoub, M. Zribi, Active/semi-active suspension control using magnetorheological actuators, *International journal of systems science* 37 (1) (2006) 35–44.
- [31] M. Unsal, C. Niezrecki, C. Crane, Two semi-active approaches for vibration isolation: piezoelectric friction damper and magnetorheological damper, in: *Mechatronics, 2004. ICM'04. Proceedings of the IEEE International Conference on*, IEEE, 2004, pp. 60–65.

- [32] P. Lischinsky, C. Canudas-de Wit, G. Morel, Friction compensation for an industrial hydraulic robot, *IEEE Control Systems* 19 (1) (1999) 25–32.
- [33] K. Khayati, P. Bigras, L.-A. Dessaint, Luge model-based friction compensation and positioning control for a pneumatic actuator using multi-objective output-feedback control via lmi optimization, *Mechatronics* 19 (4) (2009) 535–547.
- [34] Pacific Earthquake Engineering Research Center (PEER), 2011. PEER Ground Motion Database, available at <http://ngawest2.berkeley.edu/>.